

UNIVERSITY OF GENEVA

PHYSICS SECTION, DEPARTEMENT OF ASTRONOMY

BROADBAND NUMERICAL MODELING OF EXTRAGALACTIC RELATIVISTIC JETS

Aramis Raiola

LABORATORY REPORT | SUPERVISOR: ANDREA TRAMACERE
September 8, 2022

Abstract

Active Galactic Nuclei (AGN) are regions in space that host some of the most extreme conditions observed in astronomy because of the accreted matter surrounding a supermassive black hole at the centre of some galaxies. A consistent fraction among AGNs also shows the property of ejecting some of the material accreted by the black hole as two oppositely directed jets, whose travel occurs at relativistic speeds and can cover distances in the order of few Mpc. Throughout this report, we will describe the principal emission and physical proprieties of these relativistic jets, to set up a model and fit multi-wavelength Spectral Energy Distributions (SED). Using this specific model, we fitted the spectral emission of Mrk421 and compared the obtained parameters with the literature on this AGN.

1. INTRODUCTION

1.1 Preamble

Owing to the advent of radio astronomy, the sixties are considered the golden age of astrophysics. One of the most important discoveries made during those years was the first observation of "quasi-stellar radio sources", called quasars. These astronomical objects are very luminous galactic nuclei, which represent a typology of what is nowadays called an Active Galactic Nucleus (AGN). These astronomical objects are fueled by a supermassive black hole (SMBH) at their centre, whose accretion mechanisms provides for a typical structure that is shared by most AGNs (further information about AGNs composition will be given in chapter 2). A non-negligible amount of AGNs also shows a peculiar behaviour: the emission of relativistic jets. About 10% of these objects are observed to emit two ionised matter jets in opposite directions, whose spectral emission

is very characteristics and depends on different physical parameters that will be later described. The main purpose of this work is to study and analyse the broadband emission of relativistic jets and apply mathematical and numerical models to describe the spectral energy emission (SED) of these jets fitting actual astronomical data to determine the parameters proper to a relativistic jet.

1.2 Report structure

To begin with, after this introductory chapter, the main notions and mathematical tools used to characterise and study AGNs will be covered. Chapter 3 will be devoted to concretize the previously discussed theoretical aspects, by studying with the given numerical models the SED of a well known AGN: Markarian 421, and comparing the fitted parameters with the existing literature. Finally, a discussion and a concluding chapter will be devoted to drawing conclusions about the SED analysis of Mrk421.

2. THEORETICAL ASPECTS

2.1 Active Galactic Nuclei

As a result of the radio window opening during the sixties, the presence of a new kind of extragalactic radio source was detected. These astronomical objects, which are now called Active Galactic Nuclei (AGNs), are very complex systems made up of a central SMBH and the accreted matter that surrounds it. These gigantic engines, which are situated at the centre of a host galaxy, are believed to be much more energetic than the Milky Way but circumscribed within a radius that is comparable to the size of our solar system. The high power measured from these objects originates from the accretion process, which is induced by the black hole gravitational field and constrains the matter around it to be compressed and accelerated. The accreted matter is therefore heated and radiates by consequence. Moreover, some AGNs also emit two opposite relativistic jets that may also outshine the galactic nucleus itself. During the decades, astronomers were able to outline the typical structure of AGNs by analysing their emission spectrum [1].

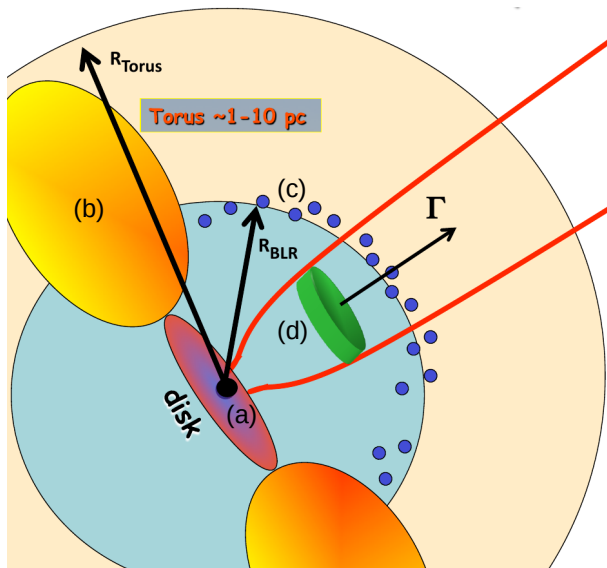


Figure 1: AGN structure scheme: (a) Accretion disk (b) Obscuring torus (c) Broad Line Region (d) Emitted blob and corresponding jet. Adapted from [2].

A general AGN is composed by a central SMBH, whose mass ranges between $10^6 M_\odot$ and $10^{10} M_\odot$. The action of the central black hole creates an accretion disk around this object, which is made up of hot spiralling matter, that emits in the UV or X-rays range. Surrounding the above-mentioned system, an obscuring torus absorbs a fraction of the radiation produced by the heated matter in the accretion disk and re-emits in the IR. The last relevant component of this structure for our purposes is the Broad Line Region (BLR), which is a zone believed to be constituted by several dust clouds in keplerian motion around the SMBH at a distance of less than 1 pc. This means that, in contrast with the Narrow Line Region (NLR) situated at hundreds of [pc] from the AGN centre, these clouds have to be circumscribed by the outer torus. These dust agglomerates absorb about 10% of the light coming from the disk and re-emit it in the visible spectrum that is observed on Earth as emission lines broadened by the relativistic Doppler effect. This description, even if widely used and accepted in literature, still presents some uncertain points. For example, the real nature of the BLR is still not understood: the observed broad lines could also be produced in the accretion disk [1]. Nevertheless, the above-mentioned description of AGNs will be considered as the standard structure of these astronomical objects. Active nuclei represent an important field in astrophysics since they are considered as sources of cosmic rays (and therefore accelerative processes), gamma-rays and extragalactic neutrinos, being then a very important source for multimessenger astronomy. Moreover, AGNs still carry several important astrophysical questions and, therefore, they are an active research field. For further description and classifications of AGNs, we need to first introduce the jet emission proprieties of Active Galactic Nuclei to better understand the detected emission on Earth. The known AGNs are distinguished by their emissions spectra, by the presence of a Jet and even by the direction toward which the jet is pointing with respect to our planet.

2.2 Relativistic Jets

2.2.1 AGNs classification by jet proprieties

From literature, it is possible to find out that the 10% of the known AGNs emit two opposite jets of ionised matter at relativistic speed. As already mentioned, this phenomenon will be at the centre of the study conducted for this report. It is however misleading to think that the phenomenon of relativistic jets can only be observed in AGNs: the emission of ionised matter jets is observed in other astronomical sources, such as micro-quasars and pulsars.

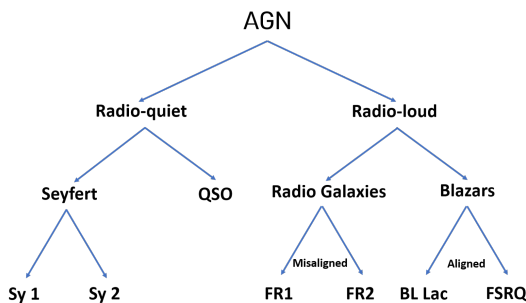


Figure 2: AGN classification depicted in a branching scheme. Radio-quiet classifications will not be considered in this work, since the main interest of the report is on Radio-loud galaxies. From [3].

In the case of Active nuclei, we exploit the presence of a jet to discern *radio-loud* active galaxies, which present the emission of a jet and *radio-quiet* AGNs, whose detected spectrum shows no sign of relativistic jet emissions. Radio loud AGNs can also be distinguished by the direction of their jets. As will be explained in the following sections, the relativistic beaming effect concentrates the angular emission of the blob at a very small angle that depends on the bulk Lorentz factor (and hence on its speed) as $\theta \simeq 1/\Gamma$. That said, radio-loud galaxies are grouped in *radio galaxies* and *blazars*. Physically speaking, radio galaxies and blazars do not present any differences, but the latter has a jet that is pointing toward Earth within its

angle of beaming. Therefore, what distinguishes the two typologies of radio-loud AGNs is the detection that we experience on the ground that, in the case of blazars, is characterised by high luminosity, high polarisation and fast variability. Another important classification is made within radio galaxies by distinguishing Fanaroff-Riley 1 (FR1) and Fanaroff-Riley 2 (FR2) galaxies which are respectively weak and powerful radio galaxies in the Fanaroff-Riley scale. To end this taxonomic description of AGNs, we can lastly separate blazars into two different kinds: BL Lac Objects and Flat Spectrum Radio Quasars (FSRQ). These two categories are believed to be the aligned counterpart of respectively FR1 and FR2 galaxies. Nevertheless, FSRQ galaxies are recognised thanks to their characteristic spectrum with spectral index $\alpha = 0$ and BL Lac Objects are typically distinguished thanks to the fact that they do not present spectral lines [3]. A scheme resuming this characterisation can be found in figure 2. Since Mrk 421 is a BL Lac Object, this group of blazars will be at the centre of the study proposed in chapter 3.

2.2.2 Jet structure and fundamental notions

Even if the mathematical models defined to describe the jet emission spectrum of radio-loud AGNs will be later explained, in this section we will focus on the definitions and basic notions about relativistic jets emitted by a radio-loud AGN. As already explained, about the 10% of the observed AGNs show the mechanism of emitting a certain amount of matter in the form of a so-called "blob" that radiates in different wavelengths while being expelled at relativistic speeds¹. These jets have sizes in the order of a few Mpc, which is far greater than the typical size of a host galaxy. The emitted blob radiates in almost all the electromagnetic spectrum, with a particular flux intensity in the optical and γ -ray band. If we study this emission in a reference frame comoving with the blob, we expect to observe an isotropic emission. On the

¹In this report, we will consider the blob as a leptonic source, without considering the hypothesis of hadronic particles within the jet.

other hand, as already mentioned, since we are observing the AGN from Earth, the emission is detected as beamed in the direction of the jet. Some structures, as radio lobes and hot spots, are believed to be generated because of the interaction with the ionized plasma of the blob and the dust present in the proximity of the galaxy. These structures are relevant since they are at rest and, therefore, their emission is isotropic. The radiation produced by radio lobes has a steep slope if plotted in logarithmic scale and, therefore, at low frequencies, the jet emission is dominated by the lobe. By analyzing the emission spectra of different radio-loud AGNs, it is possible to notice that aligned sources show a flat spectrum in the radio band (since it is the superposition of several blobs radiations) and misaligned sources present a decreasing radio spectrum, due to the fact that bigger view angles mean a decreasing beaming effect and, therefore, the predominant emission is accountable to the lobes (that, as said above, show a steep decreasing emission). Therefore, radio lobes and hot spots spectra can lead to the determination of the viewing angle of the AGN and to better define its classification. However, the most important feature of radio-loud AGNs used to study these astronomical objects is their emission spectrum analyzed in a different wavelength. In this report, we will focus on the Spectral Energy Distributions (SED) of blazars, since they represent the main topic of this work. Blazars (and in general all radio-loud AGNs) emit in almost the entirety of the electromagnetic spectrum, starting from 10^7 [Hz] to 10^{27} [Hz] for the most energetic events (which implies the detection of photons up to the range of [TeV]). The SED is often shown as the energy flux νF_ν which corresponds to the energy per unit surface and unit time, as a function of the frequency ν (always remembering that the two axes are in logarithmic scale for visual reasons). The plot of the data from a blazar presented in the typical SED axis, shows this characteristic "double-humped" pattern, as can be observed in figure 4. The first peak is believed to be the trace of synchrotron radiation of the electrons in the blob. Since the acceleration region has

a high magnetic field, electrons start spiralling around the field lines, emitting Larmor radiation. This process, known as synchrotron emission, produces a bump that usually peaks in the soft X-rays (between the MeV and GeV scale). The second peak is usually attributed to Inverse Compton (IC) effects, involving low energy photons (often referred to as *seed photons*) interacting with high energy electrons in the blob, gaining energy and being detected on Earth as the second bump in the typical blazar SED.

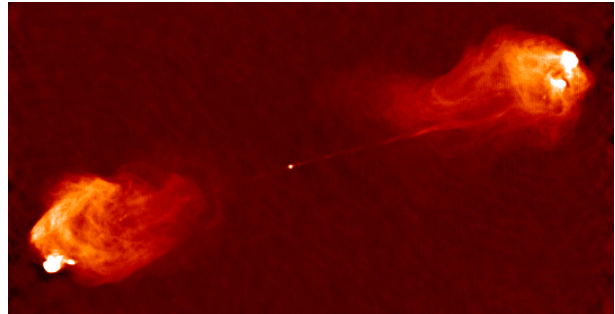


Figure 3: Cygnus A (3C 405 radio galaxy) at 5 GHz with its oppositely directed jets and radio lobes, from VLA telescope. Adapted from [4].

Even if the model involving inverse Compton is not always accepted by astrophysicists, for our purposes we will consider it as truthful. Moreover, another widely used theory, implies that the seed photons for this process are the same produced by the synchrotron emission, which seems coherent since the inverse Compton photons are the reason for the second bump, which is more energetic than the synchrotron one. This model is called Synchrotron-Self Compton (SSC). More details about these processes will be presented in the next chapter. As it is also clearly depicted in figure 4, blazars SED present high variability in time. Different periods of activity are shown in figure 4 in different colours and, by observing the effects in different wavelengths, we see that variations occur at every frequency, but high energy ranges in the SED are subjected to more drastic variations in the energy fluxes. The last fundamental aspect of blazar SED is the remarkable smoothness of the energy output, which can also be locally expressed as a power

law. This means that, if we define a generic spectral coefficient α , what we can find is that in small frequency ranges, the SED can be approximated as $F_\nu \sim \nu^{-\alpha}$. This power-law emission pattern is often associated with Fermi acceleration processes that occur in acceleration regions, such as blobs from blazars.

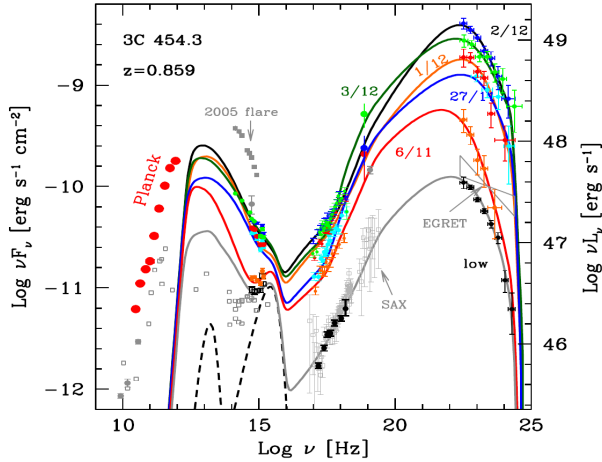


Figure 4: 3C 454.3 blazar SED analyzed for several epochs (plotted with different colors). The high variability depending on the observation time is more effective for high frequencies around the IC peak. From [4].

Blazars SED can be efficiently locally approximated by a log-parabola function. These functions are represented as parabolas if plotted in log-log axis, which can be easily adapted to the flux spectrum of radio-loud AGNs by fitting the following function with two free parameters [5]:

$$F(\nu/\nu_0) = F_0(\nu/\nu_0)^{-a-b \cdot \log_{10}(\nu/\nu_0)} \quad (1)$$

In this equation the term a is called the curvature at the peak frequency and b is the spectral index at the starting abscissa point ν_0 . The peak frequency can be determined from equation 1 as:

$$\nu_p = \nu_0 \cdot 10^{(2-a)/2b} \quad (2)$$

The study of relativistic jets, especially from radio-loud sources, is still at the beginning and, therefore, major conclusions about the composition of the blobs or the emitted power are still far from being formulated. For

instance, doubts on these subjects are supported by the uncertainties about the amount of electron-positrons pairs present in jets and the possible presence of hadronic radiation sources in the acceleration region [1]. In the next section, the mathematical tools exploited to model blazars SED fits (such as the one presented in figure 4 will be covered and, in chapter 3, the analysis of actual data from a blazar source will be presented.

2.3 Physical background

2.3.1 Relativistic effects and beaming

In this section, the main ideas about special relativity and relativistic beaming from astronomical sources will be covered. The main problem encountered when we study a jet SED, is that we are observing a source that is isotropically emitting radiations in all directions in its rest frame. When observing the source from Earth, the high speed reached by i.e. blobs is altered by relativistic effects such as time dilation, relativistic Doppler effect and light aberration. What is important to understand is that even if classical problems about relativity use the velocity of each frame as a parameter, in astronomical problems we also have to take into account the angle θ between the line of sight and the source velocity direction. To do so, it is common to regroup all these degrees of freedom in a single parameter, the relativistic Doppler factor δ :

$$\delta = \frac{1}{\Gamma(1 - \beta \cos \theta)} \quad (3)$$

where $\beta = v/c$. The relativistic transformations of several quantities in astronomy directly depend on this parameter. Precise calculations are shown in [1], where all the dependencies are calculated and justified. The most relevant transformations for this work are shown in table 1. In the next sections, the computation of synchrotron and Inverse Compton radiation will be done in the blob reference frame and the final result will be obtained by applying these transformations to the received intensity per unit frequency, in order to create a model that reproduces the observations effectuated on

Earth. However, the main relativistic effect needed in order to understand the radiation of highly relativistic sources ($\beta \simeq 1$) is the relativistic beaming effect. This phenomenon, generated by the Doppler effect and light aberration, shows the emission of an isotropic source is beamed in the direction of its velocity.

Parameter name	Transformation law
Frequency	$\nu = \nu' \delta$
Time	$t = t / \delta$
Solid angle	$d\Omega = d\Omega' / \delta^2$
Specific emissivity	$j(\nu) = j'(\nu') \delta^2$
Specific intensity	$I(\nu) = I'(\nu') \delta^3$

Table 1: Transformation from a rest frame to a generic inertial frame.

Considering a reference frame K' , where the emitting region is at rest and a frame K , where it moves with a speed $v \simeq c$, we can apply the equations for relativistic beaming that are derived in [1] to find a relation between the emission angles in the two frames, for a specific photon emitted by the source with an angle $\theta' = \pi/2$ with respect to the velocity vector:

$$\tan \theta = \frac{\sin \theta'}{\Gamma(\cos \theta' + \beta)} \Big|_{\theta'=\pi/2} = \frac{1}{\Gamma\beta} \quad (4)$$

As we can understand from equation 4, for higher velocities and, therefore, higher Γ values, we expect a smaller value of the tangent, meaning that a small angle approximation can be effectuated:

$$\tan \theta \simeq \theta \simeq \frac{1}{\Gamma} \quad (5)$$

since $\beta \simeq 1$. This means that if the observer happens to be located within an angle $\theta \sim 1/\Gamma$ with respect to the source velocity, he will measure a higher energy flux in the K reference frame since the radiation is beamed in its direction. In the context of AGNs, this scenario corresponds to the observation of a highly beamed blazar emission, as explained in the previous chapter.

²This γ Lorentz factor depends on each individual electron velocity present in the blob. It is important not to mistake it for the bulk Lorentz factor that involves the movement of the entire blob and is labelled by Γ .

2.3.2 Synchrotron radiation

The matter accreted by an SMBH, as already explained, is accelerated and heated. This system, which is at the very centre of an AGN, presents two important features: strong magnetic fields and relativistic electrons coming from the ionised matter. This combination creates the conditions needed to have synchrotron radiation. When the jet is emitted, charged particles start gyrating around the field lines and emit radiation, as expected from Larmor radiation theory (that has to be adapted to the case of relativistic leptons). From this mathematical adaptation (a complete derivation of the formula is presented in [1]) we can derive the relativistic expression for the pitch angle averaged power loss of an electron due to synchrotron radiation:

$$\langle P_s \rangle = \frac{4}{3} \sigma_T U_B c \gamma^2 \beta^2 \quad (6)$$

where σ_T is the Thompson cross-section, U_B is the energy density of the magnetic field, c is the speed of light, γ is the Lorentz factor of the electron² and $\beta = v/c$. From the single electron power loss, we can also estimate the cooling time for the synchrotron phenomenon, which is the characteristic time needed for an electron to totally radiates its energy:

$$t_{cool} = \frac{E}{\dot{E}} = \frac{E}{\langle P_s \rangle} \sim \frac{8800}{B^2 \gamma} [d] \quad (7)$$

where the power is simply defined by equation 6 and the numerator is taken to be the electron relativistic energy $E = \gamma m_e c^2$. To further proceed into the study of synchrotron radiation processes, we also have to consider that, when we are observing an astronomical source, the electrons rotating around the magnetic field lines with relativistic speeds, will have a beamed emission at an angle that is proportional to $2/\gamma$. This means that synchrotron radiation can be measured only when the charge happens to be in certain positions. As can be seen from figure 5, the detection of this radiation is only possible when the observer is positioned within an angle

of $2/\gamma$ with respect to the velocity vector of the moving charge.

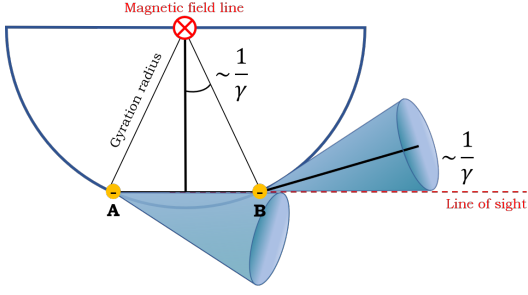


Figure 5: Electron synchrotron rotation and beamed emission scheme. Adapted from [4].

We define the typical synchrotron frequency as the frequency derived from this rotation process, also considering relativistic effects:

$$\nu_s = \frac{1}{2\pi\Delta t} = \frac{eB\gamma^2}{2\pi m_e c} \quad (8)$$

Here Δt is defined as the time needed by the electron to travel between point A and point B in the observer reference frame. At this point, we can finally enunciate³ the expression for the emitted power per unit frequency radiated by a single electron through synchrotron processes, with a defined Lorentz factor γ and a specific pitch angle θ :

$$P_s(\nu, \gamma, \theta) = \frac{\sqrt{3}e^3 B \sin \theta}{m_e c^2} F\left(\frac{\nu}{\nu_c}\right) \quad (9)$$

In equation 9 the frequency dependence is carried by the $F(\nu/\nu_c)$ function, which is often written as the integral of a modified Bessel function of order 5/3. Nevertheless, we can approximate this term as a power law multiplied by a negative exponential, that gives rise to two different regimes:

$$F\left(\frac{\nu}{\nu_c}\right) \sim \left(\frac{\nu}{2\nu_c}\right)^{1/3} e^{-\nu/\nu_c} \quad (10)$$

In this equation, we see that the presence of the emission frequency is always reduced by a term

³The mathematical steps needed to achieve this complex formulation are not presented in this report. More details can be found in [6].

ν_c^{-1} that represents a critical frequency defined as:

$$\nu_c = \frac{3}{2} \sin \theta \nu_s = \frac{3eB\gamma^2 \sin \theta}{4\pi m_e c} \quad (11)$$

As we can see in figure 6, for small frequencies values ($\nu \ll \nu_s \sim \nu_c$) we can obtain a simple power law with spectral index $\alpha = 1/3$. When the frequency increases, we then have a $F(\nu/\nu_c)$ function (and hence an emitted power) that drastically decreases as a negative exponential. Now that the power emission of a single electron can be well-defined with the previous elaborations, we need to consider the combined action of all the electrons gyrating inside the source in order to start understanding the synchrotron emissions from astronomical sources.

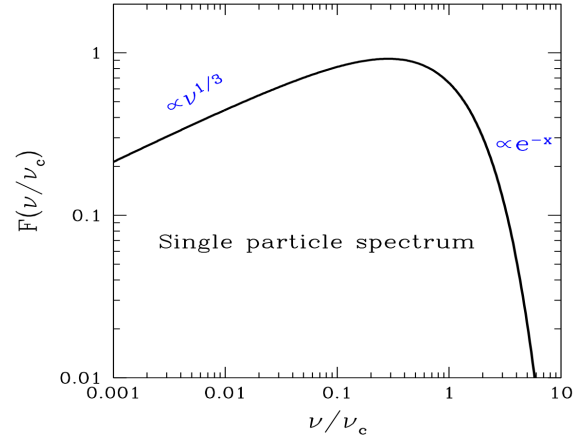


Figure 6: Single electron emission with $x = \nu/\nu_c$ in logarithmic scale. Adapted from [4].

To do so, we place ourselves in a reference frame comoving with the blob and we compute the emissivity j_ν^s , which is the power per unit surface, unit solid angle and unit frequency. Therefore, we consider an isotropic emission from the source and we integrate the power of the electron with respect to the Lorentz factor of each lepton, modulated by an electron distribution that depends on the chosen model, called $N(\gamma)$ (it is important to point out that in high-energy astrophysics, a particle Lorentz factor corresponds to an expression of its energy, since $E = \gamma mc^2$). In more pragmatic

terms, we can express the sum of all electrons contributions as:

$$j_\nu^s(\nu) = \frac{1}{4\pi} \int_{\gamma_{min}}^{\gamma_{max}} P_s(\nu, \gamma, \theta) N(\gamma) d\gamma \quad (12)$$

The values of the minimal and maximal γ and the nature of $N(\gamma)$ depends on the model we are using. Nevertheless, it is well-proven that the most typical leptonic energy distribution is the power law, as can be deduced by Fermi's theory about accelerative processes. Therefore, in order to deeper understand the synchrotron emissions from relativistic jets, we can set the electron distribution to be:

$$N(\gamma) = K\gamma^{-s} \quad (13)$$

Combining this definition of the electron distribution and the power expressed in equation 9 it is possible to find the emissivity per unit frequency using 12:

$$j_\nu^s(\nu) \sim KB^{s+1}\nu^{-\frac{(s-1)}{2}} \quad (14)$$

where K is a constant (a simple derivation of this relation is exposed in [1]). By exploiting the definition of emissivity, we can find the total flux dependencies that are expressed in equation 15. The most important feature that will have an impact on the SED shape at the synchrotron hump, is the dependency on $\nu^{-\frac{(s-1)}{2}}$. In equation 15, V represents the volume of the acceleration region (which is proportional to its radius cubed R^3) and d_L is the luminosity distance between Earth and the source.

$$F_s(\nu) = \frac{4\pi j_\nu^s(\nu)V}{4\pi d_L^2} \sim KRB^{s+1}\nu^{-\frac{(s-1)}{2}} \quad (15)$$

Nevertheless, equation 15 was determined with a simple power-law electron spectrum. In nature, this approximation with a power law is effective only at low energies, since typical distributions show a sudden drop at a cut-off Lorentz factor γ_p . This effect is associated with the cooling phenomenon that occurs at high energies and that reduces the number of highly energetic leptons in astronomical sources. Simulations with more complicated electron distributions can be found in [7]

2.3.3 Inverse Compton radiation

As was already stated, the second bump of a blazar SED is believed to be induced by Inverse Compton (IC) radiation inside the source. In this section, we aim to briefly discuss IC processes, in order to justify the mathematical explanation for the high energy part of the multiwavelength SED. This process, conversely to direct Compton scattering, involves a high energy electron that interacts with a low energy photon, conferring it a certain amount of energy that will later be detected on Earth, after the photon propagation through space. The easiest way to analyse this interaction is to think about the reference frame where the electron is at rest. In this special frame, we can calculate the energy of the incoming photon, which is predicted to later interact with the lepton through Inverse Compton scattering. If this energy is greater than the electron energy ($E_\gamma < m_e c^2$) then the electron recoil during the process can be neglected and we are dealing with the so-called: Thomson regime. In the case the photon energy is greater than $m_e c^2$, then the recoil starts to be important during the interaction and we talk about the Klein-Nishina regime. For this process, the emission power is calculated to be:

$$P_C(\gamma) = \frac{4}{3}\sigma_T c \gamma^2 \beta^2 U_r \quad (16)$$

were U_r the available energy density before the scattering. similarly to the synchrotron radiation, we also look for an overall emissivity for all the leptons present inside the source. To do so, we have to consider the electron distribution inside the source, but also the seed photons distribution depending on the specific frequency of each boson. Before doing so, we have to understand that different models for the photons distributions are possible, depending on the supposed origin of the seed photons. In the most common model, we suppose that the low energy photons available come from the synchrotron radiation, which is also taking place in the same source: the Synchrotron Self Compton (SSC) scenario. Other models suppose different interactions for example with the BLR (External Compton scenario) but, according to

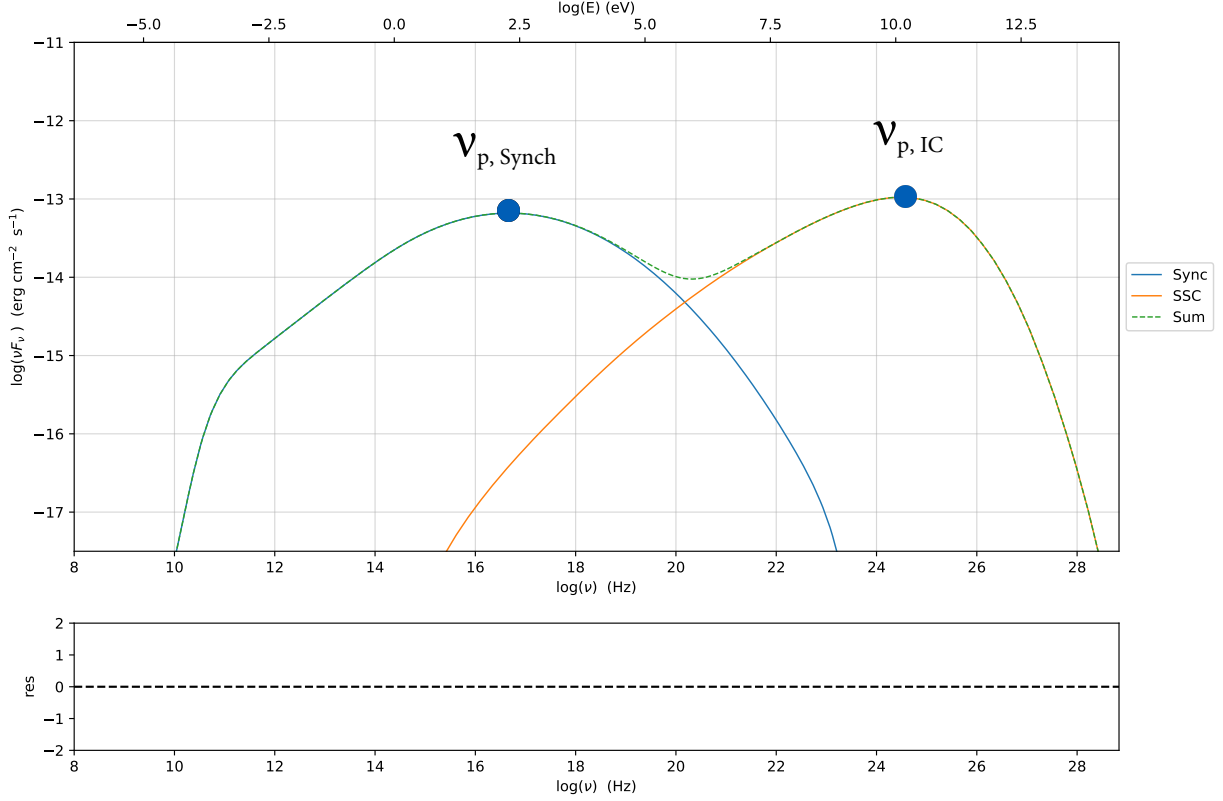


Figure 7: JetSeT plot of a SED deriving from a power log-parabola with low-energy power law branch. This simulations shows the two bumps and the corresponding peaks.

the analysis that will be done in chapter 3, we will focus on the SSC model. For this reason, we define $n(\nu_0)$ as the photons distribution within the source, and we proceed to do an integration on the photons and electrons distribution:

$$j_{\nu}^{SSC} = \frac{3\sigma_T c h \nu}{16\pi} K(\nu_0, \nu) \int_0^{\infty} n(\nu_0) d\nu_0 \quad (17)$$

with the parameter K is the integral over the electron distribution, defined in equation 18

$$K(\nu_0, \nu) = \int_{\gamma_{\min}}^{\gamma_{\max}} \frac{N(\gamma)}{\gamma^2} F_c(\gamma, \nu_0, \nu) d\gamma \quad (18)$$

In this equation, F_c is the cross-section of the interaction that depends on the frequency at which we are trying to evaluate the emissivity (ν), the seed photons frequency (ν_0) and the electrons Lorentz factor (γ). As in the synchrotron scenario, the transformation of the emissivity into the received flux on earth thanks to the Doppler factor transformations

and equation 15, it is possible to mathematically describe the second bump of the SED for many electrons. What is more important about this procedure, is that some relations between the synchrotron and IC peaks can be established. In fact, it is well-known that in a source the dominant IC regime can be determined thanks to the position of their peaks. We have a dominant Thomson regime if:

$$\nu_{p,IC}/\nu_{p,synch} \sim \frac{4}{3} \gamma_p^2 \quad (19)$$

On the other hand, we have a higher energetic Klein-Nishina regime if it is possible to verify that:

$$\nu_{p,IC}/\nu_{p,synch} \sim \gamma_p \quad (20)$$

where γ_p represents the critical Lorentz factor at which the electron distribution changes slope. In picture 7 a double humped simulated SED is displayed, along with the synchrotron and IC peaks position.

3. ANALYSIS OF MARKARIAN 421 MULTIWAVELENGTH SPECTRUM

3.1 Markarian 421 reference data

3.1.1 A brief introduction to the study of Markarian 421

In this chapter, all the efforts made in order to understand the basics behind relativistic jets emission spectra will be exploited in order to analyse with the JetSeT framework the multiwavelength spectrum of the blazar Markarian 421 (Mrk421). This AGN is a BL Lac blazar discovered in 1992 and situated at a distance of about 130 [Mpc] from Earth ($z=0.0308$). Mrk421 is one of the nearest and better-known blazars, which shows rapid emission variations and is a copious source of VHE γ -rays. The SED extrapolated from the observation of this source in different wavelengths clearly present the typical double-humped shape, with a synchrotron peak situated at 10^{17} [Hz] which places this blazar in the HBL range⁴. In literature Mrk421 IC peak is usually identified with a SSC scenario, meaning that the Inverse Compton seed photons come from synchrotron radiation [8][9]. In the first months of 2013, Mrk421 was observed in a particularly quiescent state that shifted by almost two orders of magnitudes the synchrotron peak position of this AGN. This low activity is described in the M. Balokovic et al. (2016) article [8], where multiple data taken from several ground-based and satellite telescopes (such as MAGIC, Swift, NuSTAR, Fermi-LAT) are analysed. In this article, Mrk421 multiwavelength emission is studied in 4 different periods of about 12 [hr] of exposure, between January 10 and February 12, 2013. Two among these periods are representative of the low emission state, and the other two present the data of a higher energy non-flaring state. Using the JetSeT environment, we aim to repeat the data analysis done in M. Balokovic et al. (2016) [8] starting

from the same assumptions and try to improve the obtained results. This task will be tackled through the creation of two similar models, that differs only from some adjusted parameters range, and later compared through a χ^2 test.

3.1.2 M. Balokovic et al. (2016) results

In the above-mentioned article [8], the fit of the SED data is applied following a single-zone SSC model. This means that the relativistic jet emission is considered as the result of the emission of a single spherical blob of radius R , composed of relativistic electrons whose Inverse Compton emission comes from the low energy seed photons emitted by the synchrotron process. In the article, the bulk Lorentz factor of the blob is fixed to be $\Gamma = 25$ and the viewing angle is set to $\theta = 0.04 \text{ rad} \simeq 2.29 \text{ deg}$. This is due to the fact that this angle generates a relativistic Doppler factor of 25, which makes $\delta = \Gamma$, simplifying the model.

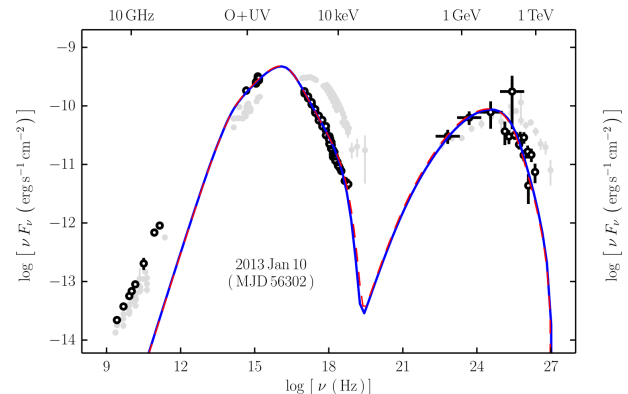


Figure 8: Fitted SED from M. Balokovic (2016) [8] for the ~ 12 [hr] observation on January 10 2013 (MJD 56302).

In figure 8 the fit on the data taken on January 10, 2013 from Mrk421 is displayed. The low-energy points are not considered into the fit, as it is usually done in research. This fact is due to the probable scenario in which the low energy points belong to the radiation of electrons coming from previously emitted blobs that are still radiating but do not represent the studied

⁴low- ν_{sync} BL Lac (LBL), Intermediate- ν_{sync} BL Lac (IBL) and High- ν_{sync} BL Lac (HBL) are further classifications of blazars that depend on the position of the synchrotron peak: respectively below 10^{14} [Hz], between $10^{14} - 10^{15}$ [Hz] and above 10^{15} [Hz]

Table 2: M. Balokovic et al. parameters for 4 periods with broken power law spectrum

Parameter	January 10	January 15	January 20	February 12
$\gamma_{\min}(10^3)$	2.0	1.3	1.7	3.0
$\gamma_{\text{brk}}(10^4)$	2.5	3.7	3.0	5.2
$\gamma_{\max}(10^5)$	4.0	4.8	5.8	6.8
p_{low}	2.0	2.0	2.0	2.0
p_{high}	4.5	4.5	4.6	4.0
B (G)	0.21	0.28	0.19	0.10
R (10^{16} cm)	0.93	0.60	1.04	1.69
L_e (10^{43} erg s $^{-1}$)	3.3	2.9	3.3	4.1
$\epsilon = L_B/L_e$	0.51	0.47	0.56	0.33
Γ	25	25	25	25
θ deg	2.29	2.29	2.29	2.29

blob. For this reason, it is reasonable to exclude them from the fit, since they do not represent the jet activity that was studied during this period, since this radiation comes from different leptons⁵. For the analysis of this model, a broken power law was defined as the energy spectrum for the electrons. This means that:

$$N(\gamma) = \begin{cases} K\gamma^{-p_{\text{low}}} & \text{if } \gamma < \gamma_{\text{brk}} \\ K\gamma^{-p_{\text{high}}} & \text{if } \gamma \geq \gamma_{\text{brk}} \end{cases} \quad (21)$$

where p_{low} represents the spectral index for low energy electrons (below the gamma-break threshold γ_{brk}) and p_{high} for high energy leptons. This approximation is often used in literature and is useful in order to compare the data with other studies about the same astronomical source (see for example [10]). In table 2 we can find the fitted values determined by M. Balokovic et al. (2016) for 4 epochs. The observation periods of January 10 and January 20 correspond to the low energy states of Mrk421, and the last two periods represent two high energy emission states (but non-flaring). From the fitted data, the synchrotron and IC peaks are found to be: $\nu_{\text{sync}} = 10^{16}$ [Hz] and $\nu_{\text{IC}} = 10^{25}$ [Hz]. This low energy state of the blazar, almost changed its classification from an HBL to an IBL, due to the influence of the very low X-ray flux of the period on the position of the SED peaks. These atypical frequencies were estimated by applying

a log-parabolic fit on each peak. From the fit it is, therefore, possible to find the ratio between the two peaks:

$$\nu_{\text{IC}}/\nu_{\text{sync}} \simeq 10^9 \quad (22)$$

Observing that $\gamma_{\text{break}}^2 \sim 10^8 - 10^9$, we can conclude (following the theory on IC radiation) that this model suggests a dominant Thomson regime for the inverse Compton process. Moreover, just by exploiting the SED peaks from the fit, it is also possible to estimate the magnetic field as follows:

$$B = \frac{4\pi m_e c \nu_{\text{sync}}}{3e\delta\gamma_c^2} \simeq 0.1[G] \quad (23)$$

This order of magnitude calculated for the blob magnetic field is concerned by the fit since this parameter was estimated to be between 0.10-0.28 G in the article. In the end, a variability time of the blazar emission was estimated to be $\tau_{\text{var}} \simeq 9[\text{hr}]$. Using this characteristic time to estimate the blob expansion, we can compute the order of magnitude of the acceleration region size:

$$R \sim c\tau_{\text{var}}\delta \simeq 10^{16}[\text{cm}] \quad (24)$$

As can be seen from table 2 the fit estimation of the parameter R is in agreement with the computation effectuated starting from the variability time.

⁵Actually, in our analysis some of the first points will be taken into account. Further explanations about this choice will be given in the next section.

3.2 Markarian 421 SED fitting

3.2.1 Main fit with broken power law

In this section, our personal fit on the same data presented in M. Balokovic et al. (2016) will be presented. This will be done by outlining the main similarities and discrepancies with the model exploited in the article and pushing forward the analysis to better understand this quiescent state of Mrk421. Even if the reference article fit of the data was effectuated with an Eyeball method, we tried to improve the results by implementing a complete numerical fit on the data, in the search of a higher precision analysis. Before studying the actual fit of the 4 periods SED, we first executed a single fit with log-parabolic functions on the two bumps separately, in order to identify the synchrotron and IC peaks frequency range. To do so, two fits with functions similar to those described in equation 1 are executed. The results for these two peaks are presented in table 3 and the plot of the poly-fit is shown in figure 9. The first remark that we can make about the results is that, simply by looking at the ν_{sync} , the January 10 and 20 observations correspond to the quiescent states of Mrk421, since the peaks are found to be around 10^{15} [Hz], which are coherent with the peaks found in M. Balokovic et al. (2016). Moving towards the remaining two epochs, we observe that the synchrotron peak frequency tends to come closer to the value of 10^{16} [Hz]. Actually, in literature, it is well known that the constraining of Mrk421 SED shows a peak at 10^{17} (see [10][11]).

Epoch	$\log_{10}(\nu_{sync})$	$\log_{10}(\nu_{IC})$
Jan 10	15.38 ± 0.03	24.06 ± 0.18
Jan 15	15.86 ± 0.04	24.40 ± 0.21
Jan 20	15.54 ± 0.03	24.52 ± 0.22
Feb 12	16.09 ± 0.04	24.89 ± 0.19

Table 3: Position of synchrotron and IC peaks for different epochs in logarithmic scale obtained with JetSeT.

This fact suggests that, even if the higher energy periods present a way higher synchrotron peak with respect to the quiescent two, we can say

that the constraining model we used shows a low activity even within the two higher energy periods. Nevertheless, the results we have are still compatible with M. Balokovic et al. (2016), which gives again a rate between the IC and the Synchrotron peak that assures a dominance of the Thomson regime for the Inverse Compton emission. At this point, we can discuss the results coming from the main fit we effectuated on the same data used for the reference article.

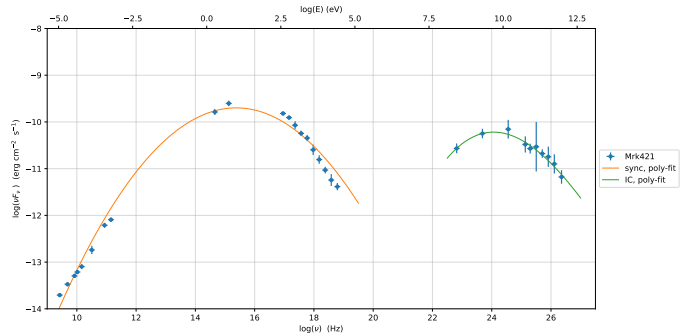


Figure 9: SED separated fit (poly-fit) of the two peaks with a log-parabola model for the synchrotron bump and a log-cubic model for the IC bump, used to determine the peaks position in the frequencies space. Fit obtained with JeTseT framework.

Nonetheless, before covering this topic, it is important to point out the main choices made before the actual constraining of the SED. Starting from raw data of the 4 epochs, we rebinned the points in logarithmic bins of size 0.2 Hz, in order to reduce the variability and homogeneity between data taken in different observation times. Secondly, we chose a fitting range going from $10^{10.5}$ [Hz] to 10^{29} [Hz]. This choice was made in order to exclude from the fit some radio points that can be regarded as the result of previously emitted blobs that create an envelop that is not compatible with the self-absorption of the source. Therefore, this emission is believed to corresponds to the deposition of older blobs along the jet, meaning that the measured radio fluxes are not coming from the same electrons as those in the synchrotron of the IC peak. Nevertheless, we made a major modification to this article approach: we chose to accept the last three low

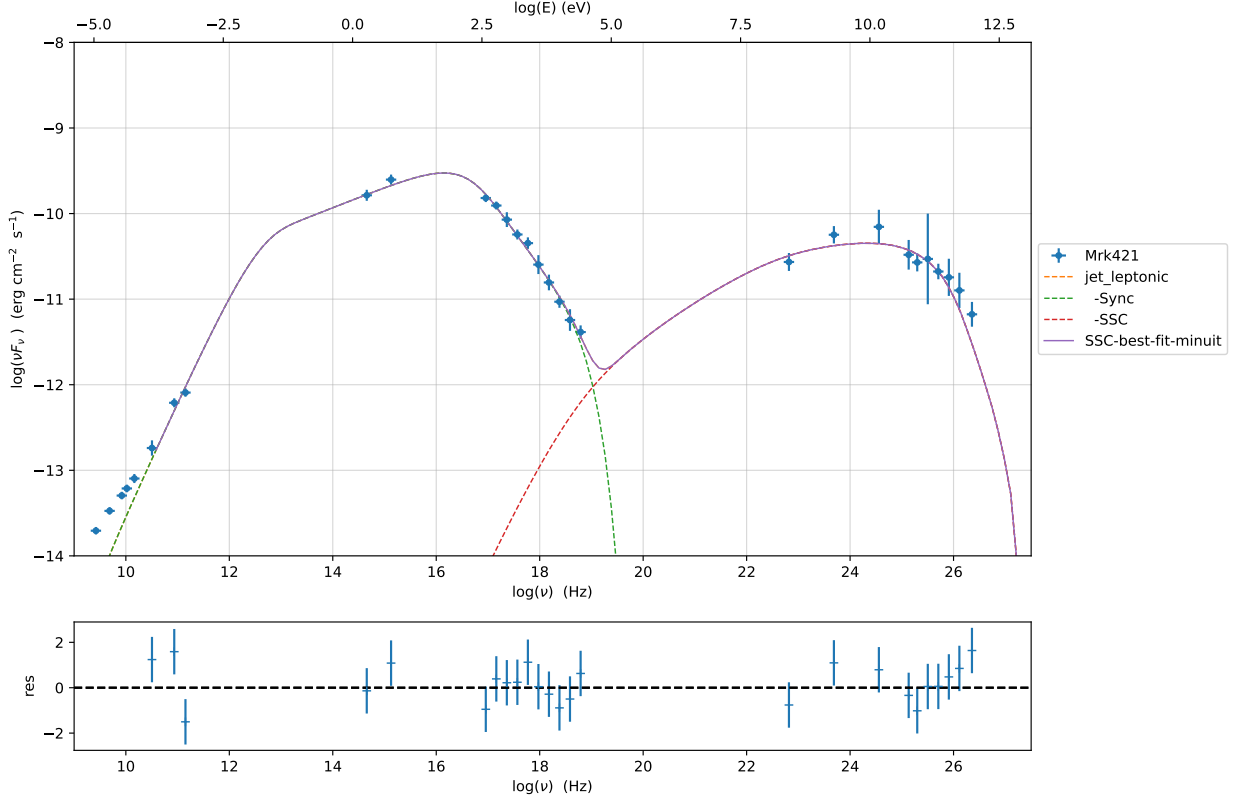


Figure 10: Complete fit of the Jan 10 epoch (MJD 56302) data with minuit minimizer applied to a SSC scenario. The axis represent $\nu F(\nu)$ as a function of ν in log-log scale. An energy scale for the detected photons can be seen above the graphic. Residuals plot are shown in the small graph below the SED. Fit obtained with JeTseT framework.

emission points, as shown in picture 10. This modification was intentionally made because we observed a remarkable spacing between these 3 points and the previous low energy points. Therefore, it is possible to suppose that these last three measurements in the radio spectrum belong to our actual blob emission and, hence, regards the same electrons as those that are contributing to the synchrotron and IC peaks. Talking about the physical properties, we chose a model according to the SSC scenario since, as mentioned above, it is the most common model used to describe Mrk421. Even if different frequencies bands (that are detected by different telescopes) have a variety of measurements time, in Balokovic et al. (2016) is specified that the soft X-rays band and the γ -rays bands data was taken in a time in the order of 12 [hr], which is the variation time we set for the analysis.

Switching now the discussion to the parameters constrain, the idea of setting $\Gamma = \delta$ in order to simplify the model was followed also for our fit (this implies imposing $\Gamma = 25$ and $\theta = 2.29$ deg). Furthermore, the cosmological redshift was fixed to its theoretical value: $z_{\text{cosm}} = 0.0308$. In order to execute the constraining on the data and optimise the fit properties, we first fitted the SED by creating a pre-fit model, that was later constrained using an lsb minimizer. This newly created model was finally fitted using a minuit minimizer, that gives a higher precision in the determination of the parameters, to the detriment of computing time. The last important remark about the fit conditions is that the parameters tuning was effectuated within certain ranges that are chosen to be coherent with the data found in Balokovic et al. (2016), in order to be able to compare the work done in

Table 4: Fitted parameters results for the 4 selected epochs SED (best-fit-minuit) considering the first fit model, without the constrain of the R-parameter. The results are fitted using a broken electron energy distribution defined between γ_{\min} and γ_{\max} with the spectral indices defined in equation 21. The asymmetric errors were estimated with a Monte Carlo Markov Chain (MCMC) sampling. For further explanations see subsection 3.2.2.

Parameter	January 10	January 15	January 20	February 12
$\gamma_{\min}(10^3)$	$0.73^{+0.05}_{-0.05}$	$0.81^{+0.06}_{-0.05}$	$0.07^{+0.00}_{-0.00}$	$0.43^{+0.03}_{-0.03}$
$\gamma_{\text{brk}}(10^4)$	$6.83^{+0.53}_{-0.63}$	$14.40^{+1.31}_{-1.09}$	$2.84^{+0.15}_{-0.15}$	$6.97^{+0.14}_{-0.19}$
$\gamma_{\max}(10^5)$	$8.19^{+0.49}_{-0.38}$	$7.95^{+0.60}_{-0.57}$	$4.84^{+0.29}_{-0.23}$	$7.71^{+0.17}_{-0.23}$
p_{low}	$2.52^{+0.06}_{-0.05}$	$2.57^{+0.04}_{-0.05}$	$1.72^{+0.02}_{-0.02}$	$2.21^{+0.04}_{-0.04}$
p_{high}	$4.65^{+0.11}_{-0.09}$	$4.36^{+0.14}_{-0.13}$	$4.39^{+0.10}_{-0.09}$	$3.90^{+0.09}_{-0.08}$
B (G)	$0.06^{+0.00}_{-0.00}$	$0.05^{+0.00}_{-0.00}$	$0.11^{+0.01}_{-0.00}$	$0.07^{+0.00}_{-0.00}$
R (10^{16} cm)	$3.80^{+0.12}_{-0.13}$	$4.59^{+0.13}_{-0.30}$	$2.28^{+0.82}_{-0.85}$	$10.00^{+0.91}_{-0.87}$
L_e (10^{43} erg s $^{-1}$)	9.68	11.40	3.09	6.65
$\epsilon = L_B/L_e$	0.14	0.10	0.48	0.13
χ^2 (dof)	18.65 (17)	31.14 (20)	10.23 (17)	10.49 (17)
χ^2/dof	1.10	1.56	0.60	0.62

the article with our personal work. We can now discuss the results from our fits on the 4 selected epochs, as done in the reference article [8], in order to analyse this quiescent state of Mrk421. At the bottom of table 4, the χ^2 and the degrees of freedom (dof) of the constrain are shown. We can deduce that, under the assumption that the model we used is accurate, the first period best-fit (January 10) better describes the data, since the χ^2 is only 1.10 times greater than the degrees of freedom. On the other hand, the fit on January 15 observations is the less accurate constrain, but $|\chi^2 - \text{dof}| \sim \sqrt{2 \cdot \text{dof}}$, which means that it should not be rejected on the basis of a χ^2 test [13]. The results are shown in table 4. In these 4 fits, we chose not to impose a restrictive fit range to the region size of the blob (R), by setting a maximum limit that ranges between 1.5×10^{17} cm and 1.5×10^{18} cm, depending on the specific fit. By comparing the fitted parameters with the values found in Balokovic et al. (table 3) we can observe that with our model many fit results are not coherent with the parameters found in the

reference article. First of all, the obtained γ_{\min} is very small with respect to the article value, with a maximal difference for the observation on February 12, where the parameter corresponds only to the 14% of article one. F On the other hand, the value for the γ_{brk} seems to be larger than what was predicted by the reference paper, with a maximal difference on January 15, with a γ_{brk} 3 times bigger than what was found in the article. For the three parameters γ_{\max} , p_{low} and p_{high} , we found out that our fit gave some values that were satisfyingly corresponding to the predicted variables. Finally, the blob magnetic field found in our model is smaller than the Balokovic et al. estimation, sometimes even by one order of magnitude. This difference between the calculated magnetic fields in the two models (and a slight difference between the electrons luminosity of the jet L_e) gave rise to a small equipartition parameter ϵ in our fit. The electrons luminosity represents the luminosity of the jet accountable for the electrons emission and the equipartition parameter is the ratio between the magnetic field luminosity

Table 5: Fitted parameters results for the 4 selected epochs SED (best-fit-minuit) considering the second fit model, constraining the R-parameter as justified in subsection 3.2.1 and reducing the number of points for the January 20 observation (the broken power law is maintained). The asymmetric errors were estimated with a Monte Carlo Markov Chain (MCMC) sampling. For further explanations see subsection 3.2.2.

Parameter	January 10	January 15	January 20	February 12
$\gamma_{\min}(10^3)$	$0.24^{+0.09}_{-0.14}$	$0.85^{+0.05}_{-0.04}$	$0.05^{+0.01}_{-0.01}$	$0.28^{+0.01}_{-0.01}$
$\gamma_{\text{brk}}(10^4)$	$2.29^{+0.11}_{-0.15}$	$5.36^{+0.29}_{-0.35}$	$2.50^{+0.09}_{-0.07}$	$5.29^{+0.33}_{-0.36}$
$\gamma_{\max}(10^5)$	$4.24^{+0.14}_{-0.14}$	$3.69^{+0.19}_{-0.21}$	$3.97^{+0.11}_{-0.13}$	$5.35^{+0.60}_{-0.46}$
p_{low}	$2.18^{+0.03}_{-0.04}$	$2.45^{+0.04}_{-0.04}$	$1.77^{+0.02}_{-0.02}$	$2.21^{+0.02}_{-0.02}$
p_{high}	$4.59^{+0.07}_{-0.08}$	$4.35^{+0.11}_{-0.11}$	$4.41^{+0.08}_{-0.07}$	$3.89^{+0.07}_{-0.07}$
B (G)	$0.21^{+0.01}_{-0.01}$	$0.23^{+0.01}_{-0.01}$	$0.21^{+0.01}_{-0.01}$	$0.15^{+0.01}_{-0.01}$
R (10^{16} cm)	$1.10^{+0.60}_{-0.20}$	$1.08^{+0.21}_{-0.21}$	$1.10^{+0.07}_{-0.16}$	$1.10^{+0.86}_{-0.18}$
L_e (10^{43} erg s $^{-1}$)	3.94	2.60	2.64	4.76
$\epsilon = L_B/L_e$	0.42	0.56	0.45	0.13
χ^2 (dof)	28.47 (17)	9.74 (12)	17.54 (17)	17.88 (17)
χ^2/dof	1.67	0.81	1.03	1.05

and L_e . These differences could arise from various elements of our model, such as the fact that we included some points into the fit that were not considered in M. Balokovic et al. or, for example, the fact that in the article an eyeball fit was used in the computation of the parameters, meaning that the precision of those could be improved by executing a numerical fit, as it was done in this report. Nevertheless, even if we have already determined a certain number of non-corresponding values, the greatest difference between the two models is represented by the region size (R), which is found to be overestimated in our model and tends to be several times bigger than the reference one. For this reason, we tried to reproduce the same fit with the same procedure adopted above, but with the only difference consisting into restraining the conditions of the fit range for the R parameter, choosing it to be between $10^{15.5}\text{cm}$ and $1.1 \times 10^{16}\text{cm}$. With this newly-defined model, we aim to understand if underestimating the region sizes for the 4 epochs could lead to results closer to those

found in the reference article and if the χ^2 value of these fits could be closer to the degrees of freedom, causing this second model to be the better-describing one. In addition to this new definition of the R -parameter limits, we also applied a modification to the fit of the observation time on January 15. Since the high energies flux is increasing around the highest frequencies of the SED, we decided not to take into account these points, placing this specific epoch fit range to 10^{26} [Hz]. This high valued flux can be accounted as an anomaly in the VHE γ -photons production from the source but, since we are facing an atypical behaviour, we excluded those points from the fit. We can now comment on the fit results, starting with the ratio between the χ^2 values and the degrees of freedom. The results presented at the bottom of table 5 clearly show that for the last three periods, the value of χ^2/dof has improved, especially for the last two fits, where it almost converges to 1.00. Nonetheless, the first observation period showed an increase of χ^2 with this model, suggesting that the fit from the previous jet modelling better

described this data set. However, we can state that for the last three fits the χ^2 test implies that the "reduced-R" model better fit the observed emission flux of Mrk421 in the 4 observation epochs. The results from the fit presented in table 5 directly show some improvements with respect to the previously determined parameters (table 4), always comparing the constrained values with table 2. First of all, the previously determined low magnetic field (found via the first model fits) is now coherent with the B-parameters found in M. Balokovic et al., also showing a consistent reduction of the magnetic field during the last epoch, as found by our data analysis and in the reference article. We might now shift the focus to the electron distribution: the γ_{brk} is now more in agreement with the reference article since we solved the problem concerning the January 15 observation parameter, which was one order of magnitude greater than the article one. Even if γ_{max} values were already compatible with the article, this new model slightly improves the similarity with the M. Balokovic et al. values. Nevertheless, it was not possible to fix the problem with the small γ_{min} parameters, that seem to be too small. This result could be influenced by the fact that in our model, we still considered some of the low energy points as proper to the synchrotron bump, affecting the low energy range of the electron distribution. However, this parameter is typically very difficult to determine with precision but, in this case, in literature, it is also possible to find values that are closer to the order of magnitude we found via the SED fitting with our models (see [10] and subsection 3.2.3 for a more detailed discussion). Moreover, as also found with the previous analysis, the values of the spectral indices of the electron distribution are always coherent with the predicted values, indicating that these parameters are well defined, regardless of the chosen model. Finally, also the electrons luminosity better fits the values found in M. Balokovic et al., showing that the second model is in agreement with the reference fit and consequently improving the correspondence with the equipartition parameter. Obviously, no discussion can be made on the region size R,

since the fit value is found on purpose at the higher bound of the given range, to reduce this parameter and better fitting the data (we also find a big error on this value, since it is too constrained). The choice of exploiting the second model was not effectuated to merely reproduce the results from M. Balokovic et al., but it was done in order to found better values for the magnetic field, whose order of magnitude is calculated in equation 23, in agreement with the synchrotron peak position in the frequency space. Moreover, as already stated, the second model improves the χ^2 -value, which helps us execute a χ^2 -test that found the second model to be more consistent with the measured data. In the next subsection, before commenting on the results and analysing the 2013-quiescent state of Mrk421 with the help of the reference article, the parameters errors calculation will be presented, in order to understand how they were estimated.

3.2.2 MCMC and errors determination

All the parameters that were presented before (except the electrons jet luminosity) show 2 symmetric or asymmetric, negative and positive errors. This estimation was made following a Monte Carlo Markov Chain (MCMC) algorithm applied to our parameters space. Even if we will not enter into all the details about this important topic in statistics, MCMC algorithms are used to approximate the expectation and the distribution of an arbitrary random variable distributed with a complicated probability distribution in an n-dimensional space. Generally, this group of algorithms samples some points with a random walk that accepts the points with increasing probability, in order to only account for the high-probability points in the parameters space, which are the most influential in the random variable mean value determination. JetSeT offers an MCMC implementation to further study the best-fit parameters, based on the Metropolis–Hastings algorithm. This procedure uses a non-informative prior distribution (flat in our case) centered on the best fit values provided by minuit and with a dispersion equal to N times the error provided by minuit. The

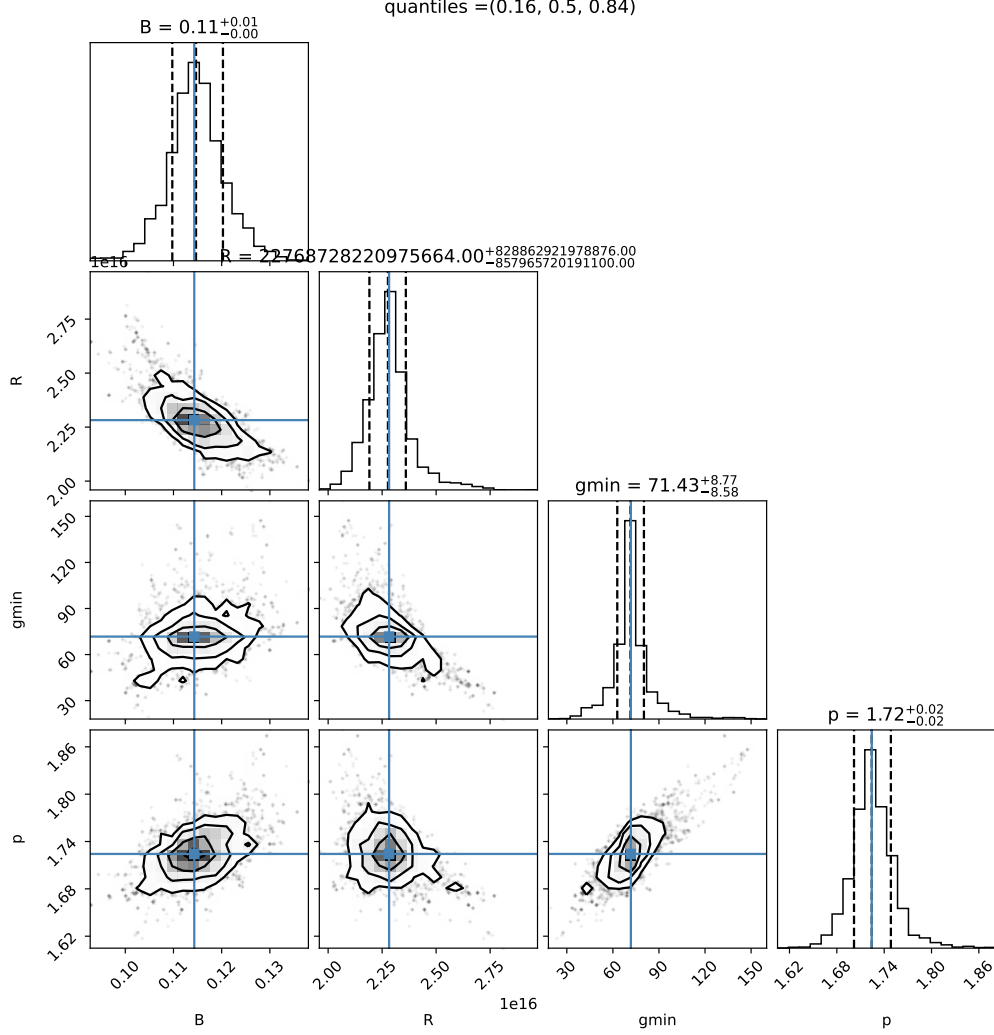


Figure 11: JetSeT corner plot for three chosen parameters from the first fit model (with no reduction of the R range) applied to the January 20 data. It is possible to observe e.g. that the parameters γ_{min} and p are correlated and that no correlation seems to appear between the region size R and p .

algorithm generates a random walk in the distribution space, accepting or rejecting jumps to new positions based on the 'likelihood' of the sample, and provides an estimate of the posterior distribution of the parameters. We can use the posterior distribution to estimate the confidence interval for each parameter of the fit, that is the method followed in the previous chapter to estimate the asymmetric errors reported in the Table 5 and 4. From this algorithm, we can also derive some corner plots, such as the example displayed in figure 11. In this typology of plots, we see the joint estimated

probability distribution in the parameters space, which leads to some deeper interpretation of the data following the chosen model and starting, in this case, from the best-fit-minuit. In fact, observing a linear trend between two parameters implies a degeneracy among parameters, that can be interpreted as a correlation between the two. From the probability distributions of the parameters, we can then determine the 1- σ confidence intervals. In figure 11, the plots on the diagonal of the corner plot show the sampled probability distribution for the specific parameter, together with the best fit value

(blue vertical solid line) and the $1\text{-}\sigma$ confidence boundaries (black vertical dashed lines).

3.2.3 Four epochs fit discussion

To review the analysis effectuated so far, we can state that the main accomplished task was to create two single-zone SCC models with JetSeT, following the study carried out by M. Balokovic et al., with the simplification of a broken power law as the electron distribution and the definition of $\Gamma = \delta$, in order to fit the SED of Mrk421 jet during four epochs.

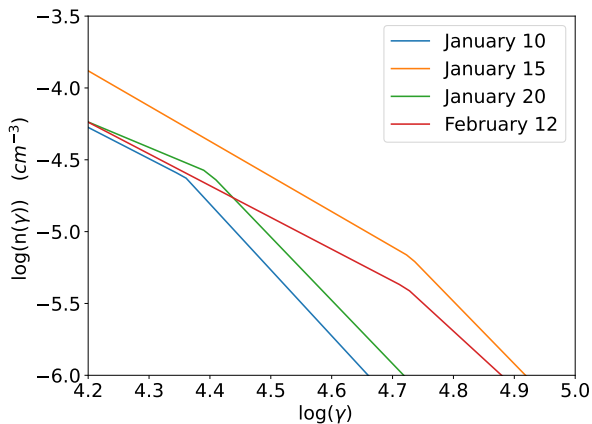


Figure 12: Electron broken distribution around γ_{brk} , showing a remarkable difference between the critical points of the low energy periods and high energy observations. Simulation effectuated with JetSeT on the basis of the fit parameters.

In contrast to the reference article model, we also chose to fit some low energy measurements, since their higher position in terms of flux suggests that they are proper to the contemporary blob. The difference between the two created models is that in the second one we reduced the fit range for the R-parameter, in order to find results that better correspond to the reference paper and that gave more respectable χ^2 values for the fit. Therefore, in this results discussion we will give higher importance to the second model, presented in table 5. The data sets are separated into 2 low energy quiescent states of Mrk421 (January 10 and 20) and two higher energy, but non-flaring states (January 15 and February 12). What we observed in table 3 is that the synchrotron and IC peaks are shifted to lower frequencies during the observation periods

in 2013 for each one of the 4 epochs, since Mrk421 is usually observed having a synchrotron peak at 10^{17} [Hz]. Moreover, during the two low-energy periods, we also observed that the peaks were so shifted down, that Mrk421 almost changed its classification into an IBL blazar, even though it is well known to be one of the HBL blazars par excellence. The second important observation is related to the region size and the magnetic field of the blob. What we found in this data analysis was that an underestimation of R gave a higher evaluation of the overall magnetic field for the 4 epochs. Also using the MCMC, we observed that we have an inverse correlation between the R-B parameters, showing that these two quantities are inversely proportional in our model. Even if the second model seems to better represent the data following a χ^2 test (at least for the three last periods), an article from 2011 about Mrk421 [10] found some values closer to our first model (4): e.g. a magnetic field of 0.038 G and an equipartition parameter of about 0.1. Nevertheless, the analysis of Mrk421 was not effectuated during the same period and the model chosen for [10] was a double broken power-law spectrum, with two different γ_{brk} . Finally, we can discuss the parameters related to the electrons energy distribution. We observed that we found a very small value of γ_{min} which, as said before, could be an effect driven by the incorporation of three lower energy points in the SED fit. Even though these values were particularly small, we could observe that the two low energy epochs presented a smaller γ_{min} value. Nonetheless, the January 10 parameter had a big error determined via the MCMC, generating some doubts around this assertion. However, the most remarked difference between the low energy states and the high activity periods is the position of the critical Lorentz factor γ_{brk} . By looking at table 5, it is clear that the value of this parameter is more than doubled when reaching a high energy epoch, as shown in a simulation displayed in figure 12. For this reason, we can state that the critical Lorentz factor is the key parameter in order to understand the difference between the quiescent and higher energies states.

4. CONCLUSIONS

Relativistic jets astronomy represents a fundamental topic in high-energy astrophysics, due to the open questions that are still surrounding this ongoing research field. The selected subject is a astrophysical studies were special relativity, electrodynamics and particle physics are exploited in order to understand the structure of AGNs and try to solve some of the questions that are still unanswered about the accretion mechanisms or AGNs structure. During this report, we had the opportunity to explore this topic and to understand the basic physics behind these extreme phenomena. To summarise: throughout this report, in the first chapters, the fundamental AGN jets astronomy theory and the mathematical models used to explain the SEDs observations on Earth were covered. Eventually, we used this knowledge to analyse the SED of Mrk421 during the first period of 2013, following the study effectuated by M. Balokovic et al. in 2016 [8]. At the beginning of 2013, Markarian 421 was found to be in one of the lowest energy quiescent states of its observation history. With the JetSeT framework, it was possible to fit the SED of four selected observations epochs between January 10 and February 12, 2013 and draw some conclusions. Aiming to improve the eyeball constrain executed in the reference article, we implemented a numerical fit by the introduction of two similar models, that differed by the constraints applied to the region size. With these two models, we found out that during 2 among these 4 periods, Markarian 421 showed a synchrotron peak shifted by practically two orders of magnitudes, almost changing its classification into an IBL blazar. This fact suggests that categorising blazars depending on the synchrotron peak frequency is a valid choice only for defined periods of time, since the high variability of blazars can induce the classification to be not consistent anymore after a certain amount of time. Secondly, it turns out from our analysis that the main difference between low energetic and high energy epochs seems to be found in the electrons energy distribution where,

for instance, quiescent states of Mrk421 show lower γ_{brk} values. To conclude, at the end of this work we can state that the theoretical aspects covered and the analysis effectuated clearly show that the study of astronomical objects SED, at least in the case of relativistic jets, followed by the application of the previously discussed mathematical models, can be a source of an astonishing amount of information about the source. Using a numerical fit model, it was possible to further analyse the data and furnish a more precise estimation of the blazar parameters, also adding some confidence intervals on the calculated quantities. Even if we are still far from having a complete understanding of relativistic jets in astronomical sources, the models we have developed so far seem to present good results to determine the main parameters involved in the idealisation of these sources.

As already mentioned, all the fits and analysis presented in this report were made using the JetSeT framework (all the features of this environment can be found in [7]). The code that was used to produce the fits and the MCMC is published on a github repository in the form of Jupyter notebooks at this [address](#).

REFERENCES

- [1] G. Ghisellini, *Radiative Processes in High Energy Astrophysics*, Lecture Notes in Physics, Springer International Publishing, [arXiv:1202.5949](#) (2013)
- [2] A. Tramacere, *Numerical modelling of radiative and accelerative processes with the JetSeT code*, University of Geneva, (2020)
- [3] C. D. Dermer, B. Giebels, *Active galactic nuclei at gamma-ray energies*, C.R Physique 17, [Elsevier](#), 594-616(2016)
- [4] C. L. Carilli, P. D. Barthel, *Cygnus A*, The Astronomy and Astrophysics review, Springer-Verlag, [A&A](#) (1996)
- [5] E. Massaro, A. Tramacere et al, *Log-parabolic spectra and particle acceleration in blazars*, [A&A](#), 448, 861–871 (2006)

- [6] K. Wille, *Synchrotron radiation*, Technical University of Dortmund, Joint University Acceleration School, lecture notes (2013), [CERN Indico](#) pp. 30-31.
- [7] A. Tramacere, SED modeler and fitting Tool (JetSeT), version 1.1.2, [JetSeT documentation](#), last consulted on 30.07.2021
- [8] M. Balokovic et al., *Multiwavelength study of the quiescent states of Mrk421 with unprecedented hard X-Ray coverage provided by NuSTAR in 2013*, [arXiv:1512.02235](#), ApJ 819:156 (2016)
- [9] I. Donnarumma, *The blazar Mrk 421: a short multifrequency review*, [ads](#), Mem. S.A.It. Vol. 83, 122 (2012)
- [10] A.A. Abdo et al., *Fermi-LAT Observations of Markarian 421: the Missing Piece of its Spectral Energy Distribution*, [arXiv:1106.1348](#), ApJ, 736, 131 (2011)
- [11] M. Ushio et al., *A novel approach in constraining electron spectra in blazar jets: the case of Markarian 421*, [arXiv:1009.2666](#), ApJ, 724, 1509 (2010)
- [12] A. Tramacere, *JetSeT documentation*, Model fitting 1: Only SSC, [JetSeT 1.2.0rc8](#), last consulted on 22.07.2021
- [13] D.W. Hogg et al., *Data analysis recipes: Fitting a model to data*, [arXiv:1008.4686v1](#), astro-ph.IM (2010), p.51